nature portfolio

https://doi.org/10.1038/s41567-021-01438-2

Supplementary information

Moiré nematic phase in twisted double bilayer graphene

In the format provided by the authors and unedited

Supplementary Information for Moiré nematic phase in twisted double bilayer graphene

Carmen Rubio-Verdú[1]*, Simon Turkel[1]*, Yuan Song[1], Lennart Klebl[2], Rhine Samajdar[3], Mathias S. Scheurer[3,4], Jörn W. F. Venderbos[5,6], Kenji Watanabe[7], Takashi Taniguchi[8], Héctor Ochoa[1], Lede Xian[9,10], Dante M. Kennes[2,9], Rafael M. Fernandes[11], Ángel Rubio[9,12,13], Abhay N. Pasupathy[1†]

[1]Department of Physics, Columbia University, New York, NY 10027, USA
[2]Institute for Theory of Statistical Physics, RWTH Aachen University, and JARA Fundamentals of Future Information Technology, 52062 Aachen, Germany
[3]Department of Physics, Harvard University, Cambridge, MA 02138, USA
[4]Institute for Theoretical Physics, University of Innsbruck, A-6020 Innsbruck, Austria
[5]Department of Physics, Drexel University, Philadelphia, PA 19104, USA
[6]Department of Materials Science and Engineering, Drexel University, Philadelphia, PA 19104, USA
[7]Research Center for Functional Materials, National Institute for Materials Science, 1-1 Namiki, Tsukuba 305-0044, Japan
[8]International Center for Materials Nanoarchitectonics, National Institute for Materials Science, 1-1 Namiki, Tsukuba 305-0044, Japan
[9]Max Planck Institute for the Structure and Dynamics of Matter, Center for Free Electron Laser Science, 22761 Hamburg, Germany
[10]Songshan Lake Materials Laboratory, 523808 Dongguan, Guangdong, China
[11]School of Physics and Astronomy, University of Minnesota, Minneapolis, MN 55455, USA
[12]Center for Computational Quantum Physics (CCQ), The Flatiron Institute, New York, NY 10010, USA
[13]Nano-Bio Spectroscopy Group, Departamento de Física de Materiales, UPV/EHU, 20018 Donostia, Spain

* These authors contributed equally to this work.
† Corresponding author: apn2108@columbia.edu

1. Continuum model LDOS under an external displacement field.

As described in the main text, the back gate voltage in the STM geometry introduces charge doping as well as a transverse displacement field. The presence of a finite displacement field has the effect of creating a layer-dependent electric potential, which can be captured within the continuum model by including layer-dependent on-site energies Δ(z). In order to quantitatively determine the effect of the displacement field on the single particle band structure for the experimental range of gate voltages, we self-consistently compute the on-site energies Δ(z) for each experimental displacement field using the method outlined in Ref. 1. Beginning with an assumed set of layer potentials $\Delta(z) = zD/\varepsilon$, where we take $\varepsilon \sim 12$ as the dielectric constant of the double-bilayer stack, we solve for the charge density n(z) on each layer. The resulting electrostatic potential is given by the sum of the external displacement field and the field due to the redistributed charge densities n(z) and gives rise to a new set of layer potentials, Δ'(z). To enforce the self-consistency condition, we iterate this procedure until each Δ'(z) matches the corresponding input Δ(z) to within 1 meV. The calculations presented in the main text use this converged set of layer potentials.

The resulting top layer projected densities of states from this self-consistent calculation for several displacement fields are shown in Fig. S1 (right) beside the corresponding experimental spectra (left). We find that this procedure for determining the on-site potentials provides a quantitative description of the experimental curves. We note, in particular, that for negative displacement field the valence flat band appears to split both in experiment and in the single-particle calculation. This apparent splitting is a single-particle effect due to the displacement field sourced by our gate electrode and the resulting redistribution of the density of states onto the top layer.

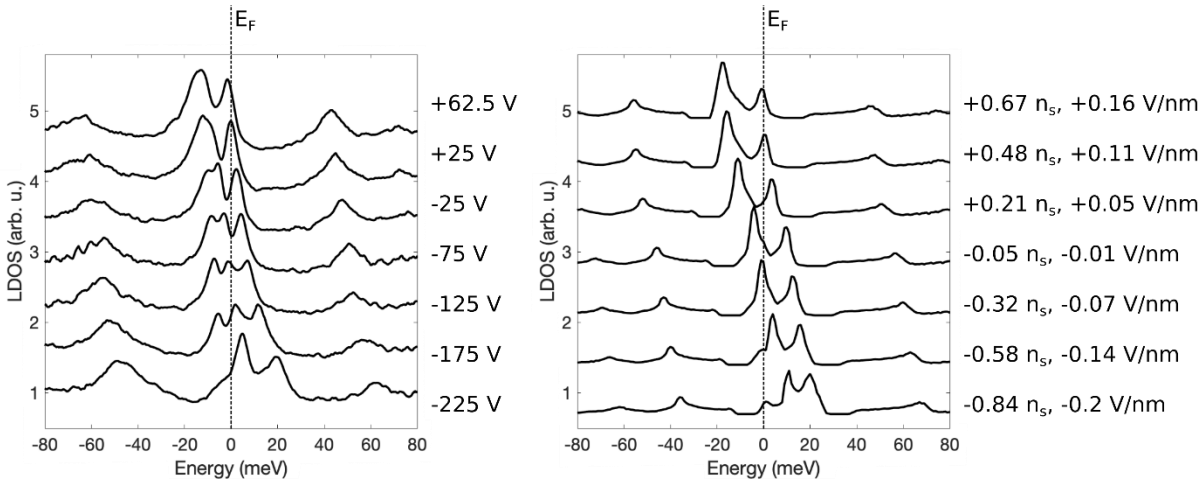

Supplementary Figure 1. 1.05° TDBG under the presence of a displacement field. (left) Experimental spatially-averaged LDOS of TDBG at several back-gate values. (right) Continuum model DOS projected onto the top layer under the presence of a displacement field. The doping and displacement field values are included. The vertical dashed lines indicate the Fermi level.

2. Direct evidence of primary nematic order

A perennial problem in the experimental characterization of nematic order in crystalline solids concerns the microscopic origin of symmetry-broken phases. The relevant question is whether broken symmetries are driven by changes in the structural morphology of the crystal or rather by electronic correlations[1]. In twisted graphene, this question becomes particularly important due to the presence of varying amounts of heterostrain across experimental devices. It has been shown, for instance, that small amounts of heterostrain in twisted bilayer graphene can stabilize symmetry-broken phases even in the absence of a primary nematic order[2]. The distinction between long-range nematic order or large nematic fluctuations that condense in the presence of external strain is therefore highly important in the context of understanding the electronic properties of real devices, as it implies that small variations in strain between samples can lead to significant differences in their respective ground states.

One way to experimentally disambiguate between these two possible scenarios is by examining the dependence of the nematic order parameter on externally applied strain. If there is spontaneous nematic long-range order, then we expect that the amplitude of the

nematic order parameter will not be very sensitive to strain deep in the ordered state. On the other hand, if the system were characterized by a large nematic susceptibility but no spontaneous nematic order, then we would expect to see a roughly linear response of the nematic order parameter to applied strain at small strains. While it is technically challenging to controllably apply strains to twisted heterostructures in an STM measurement, the random distribution of built-in strains that we observe between different samples nevertheless allows us to passively probe the effect of strain on the nematic order.

In addition to the sample presented in the main text (Sample 1), we have performed STM measurements on a second sample (Sample 2) with similar symmetry breaking phenomenology. Fig. S2 shows large area LDOS maps of Sample 2 displaying a uniform moiré pattern corresponding to a twist angle of 1.1˚. LDOS maps acquired in the valence flat band, where symmetry breaking was most pronounced in Sample 1, are shown for dopings of $n_s/2$ (Fig. S2b) and charge neutrality (Fig. S2c). As in Sample 1, we find that the LDOS at $n_s/2$ breaks the C_3 rotational symmetry that was present at charge neutrality.

As described in the main text, we quantify the local heterostrain in our samples by fitting STM images with two dimensional Gaussian functions to extract the precise BAAC site positions (Figs. S3a and S3b). Figs S3c (Sample 1) and S3d (Sample 2) show the three principal moiré lattice vectors extracted from BAAC site positions and each rotated by 0˚, 60˚, and 120˚ respectively from their original orientations to facilitate comparison. In the case of zero external strain, the three vectors for each sample would align identically. The amount of spread between the endpoints of these vectors corresponds directly to the magnitude of heterostrain present in the given sample. Since the heterostrain in our samples is generally small (<0.5%), each bilayer is expected to stay locked in the Bernal configuration[3], so that we can compute heterostrain using the procedure outlined in Ref. 5 for twisted bilayer graphene, with the sole exception that strain is here understood to be applied uniformly to each Bernal bilayer. From this we obtain heterostrain values of 0.03% and 0.12% for Samples 1 and 2 respectively.

The fourfold difference in heterostrain magnitude between Samples 1 and 2 would produce a comparable difference in the strength of the nematic order parameter if the observed symmetry breaking were a result of external strain combined with a large nematic susceptibility. On the contrary, we observe practically no difference in the strength of nematic order between these two samples. Figs. S3e and S3f show single moiré unit cell LDOS maps at energies in the valence flat band acquired on Samples 1 and 2 respectively. Each map was acquired when the sample was doped to half filling of the conduction flat band ($n_s/2$), where the observed nematic order is strongest. As in the main text, we quantify the strength of the nematic order by subtracting rotated versions of the LDOS images and summing the result[4]. In the case of perfectly C_3 symmetric images, the output of this procedure would be identically zero. The finite nematic order, however, produces finite anisotropy values of 34.9% and 35.6% in Samples 1 and 2 respectively. These nearly identical anisotropy values in two samples with a fourfold difference in heterostrain demonstrate the insensitivity of the nematic order to small applied strains. This suggests that the observed symmetry-broken phase is the result of a spontaneous rather than explicit symmetry-breaking.

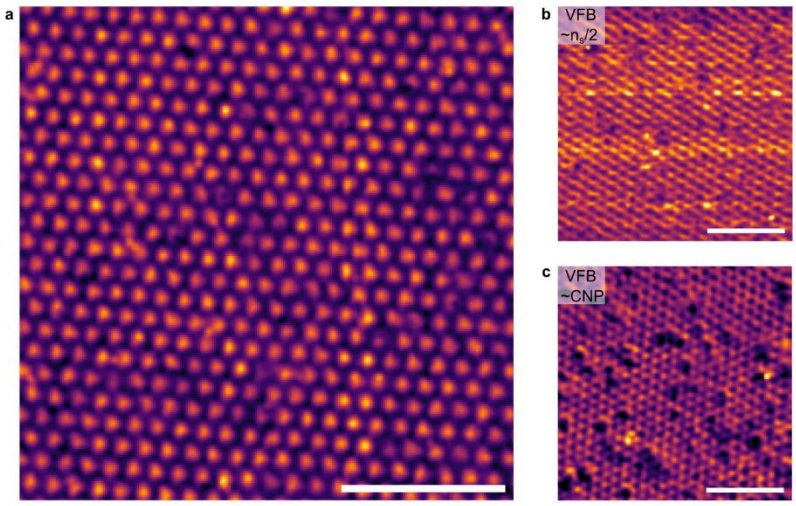

Supplementary Figure 2. Twisted double bilayer graphene at 1.1° twist angle. **a**, STS LDOS map on a 300x300nm^2 region of uniform moiré. **b**, **c**, STS LDOS map on the same region as a, at the energy of the valence flat band and at half-filling and charge neutrality point, respectively. Scale bars correspond to 100 nm.

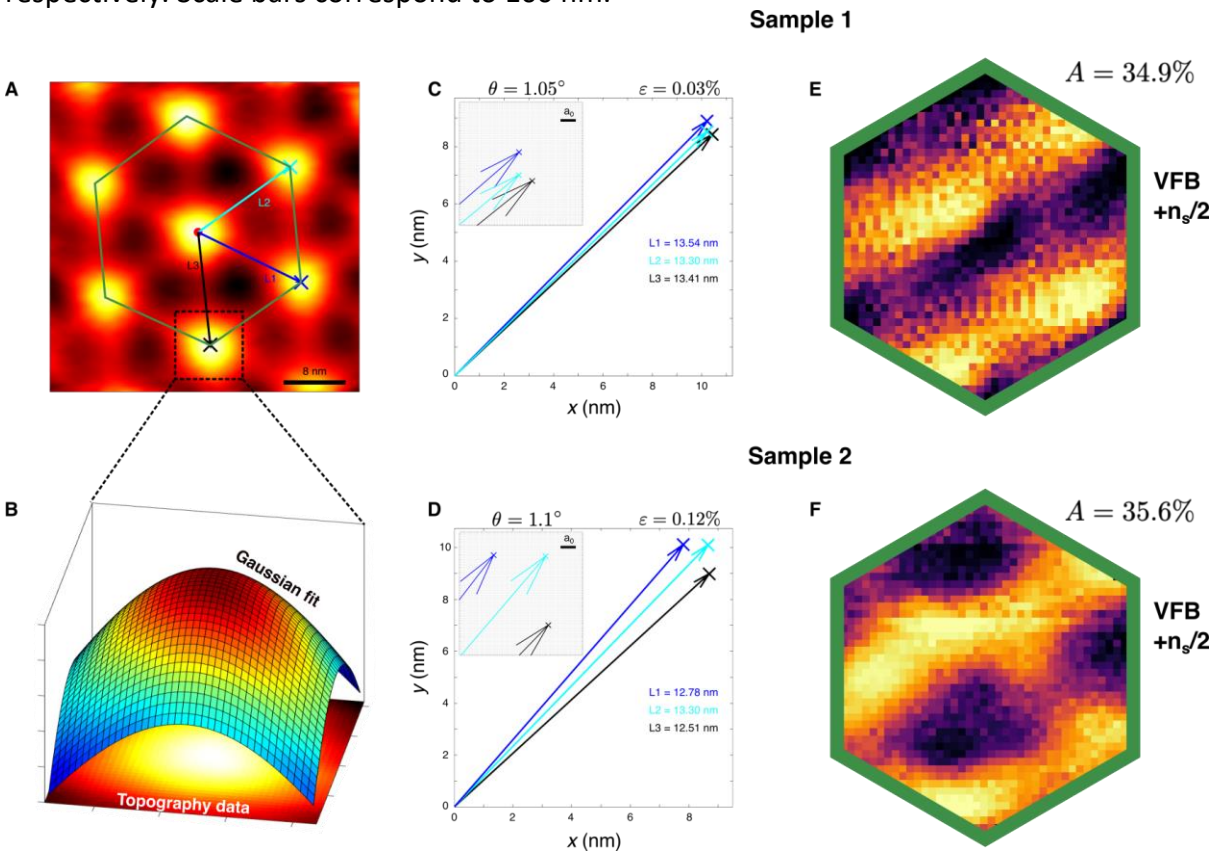

Supplementary Figure 3. Comparing broken symmetry for different heterostrains. **a**, STM topograph of a single moiré unit cell of TDBG at a twist angle of 1.05˚. Moiré lattice vectors are shown as arrows connecting adjacent BAAC sites. **b,** Illustration of Gaussian fit used to

identify BAAC site positions for twist angle and strain quantification. **c** and **d,** Moiré lattice vectors for Samples 1 (c) and 2 (d), each rotated by 0˚, 60˚, and 120˚ to facilitate comparison. The heterostrain magnitudes correspond to the spread of the endpoints of these vectors. **e** and **f,** LDOS maps acquired in the valence flat band (VFB) and at half filling of the conduction flat band (+n_s/2) for Samples 1 (e) and 2 (f). To emphasize the symmetry breaking, each map is cropped to a single moiré unit cell, shown as the hexagonal green outline in (a).

3. Tight-binding Model.

The band structure of TDBG is microscopically generated from a tight-binding model as presented in Ref. 5. We use a commensurate atomic structure with a twist angle of $\theta \approx 1.1^\circ$ that has 22328 sites per unit cell. The atomic structure is relaxed using the LAMMPS code[6] with the same parameters as described in Ref. 8. The intralayer interactions within each graphene layer are modeled via the second-generation reactive empirical bond order (REBO) potential[7]. The interlayer interactions are modeled via the Kolmogorov-Crespi (KC) potential[8], using the recent parametrization of Ref. 11. The relaxation is performed using the fast inertial relaxation engine (FIRE) algorithm[9]. We set the hopping parameters to $V^0_{pp\pi} = -3.24\text{eV}$ and $V^0_{pp\sigma} = 0.48$ eV which reproduces our experimental findings of the LDOS well. The intrinsic symmetric polarization energy (on-site potentials for the inner layers) is set to -32.76 meV. This value is chosen to obtain consistent results with DFT simulations. The non-interacting part of the Hamiltonian then reads

$$\mathcal{H}_0 = \sum_{i,j,\sigma} V_{ij} c^\dagger_{i,\sigma} c_{j,\sigma} \qquad \textit{Eq. 1}$$

where V_{ij} denotes the resulting hopping amplitude between sites i and j and $c^{(\dagger)}_{i,\sigma}$ annihilates (creates) an electron on site i with spin σ. We use an Ohno type interaction[10] that is screened for $r = 0$ and truncated by either a smooth Fermi cutoff function at $r_c = 2a = 4.9$ Å $\left(C_f(r) = \left[\exp\left((r - r_c)/0.2a\right) + 1\right]^{-1}\right)$ or a sharp cutoff function at $r_c = 1.5a = 3.69$ Å $\left(C_s(r) = \Theta(r_c - r)\right)$. The interacting part of the Hamiltonian with an interaction range cutoff $C(r)$ then reads

$$\mathcal{H}_{int} = \sum_{i,j,\sigma,\sigma'} \frac{UC\left(|\boldsymbol{r}_i - \boldsymbol{r}_j|\right)}{\sqrt{1 + \left(\left(\boldsymbol{r}_i - \boldsymbol{r}_j\right)/r_s\right)^2}} \rho_{i,\sigma}\rho_{j,\sigma'} \qquad \textit{Eq. 2}$$

with the density-operator $\rho_{i,\sigma} = c^\dagger_{i,\sigma} c_{i,\sigma}$ and $r_s = 3a = 7.38$Å. For our functional renormalization group (fRG) simulations, we set the interaction strength to $U = 3$ eV and $U = 4$ eV (with a smooth Fermi cutoff at $r_c = 2a$) and $U = 6$ eV and $U = 8$ eV (with a sharp cutoff at $r_c = 1.5a$).

The effect of small heterostrain can be analyzed using the non-interacting part of the tight-binding model defined in the previous section. To consider small strain values comparable to experiment, we slightly scale the graphene lattice vectors of one of the two AB stacked bilayer graphene sheets. In particular, we first twist the top two layers by $\theta \approx 1.1^\circ$. Then we impose a small amount of uniaxial heterostrain by slightly expanding the lattice constant of the top two layers along one of the lattice vectors ($\mathbf{t}_{t2}$) by ~0.1%. The resulting moiré supercell lattice vectors ($\mathbf{t}_{s1}$,$\mathbf{t}_{s2}$) can be represented as: $\mathbf{t}_{s1}$=30 $\mathbf{t}_{t2}$ + 32 $\mathbf{t}_{t1}$=29 $\mathbf{t}_{b2}$ + 33 $\mathbf{t}_{b1}$; $\mathbf{t}_{s2}$=31 $\mathbf{t}_{t2}$ +29 ($\mathbf{t}_{t2}$-$\mathbf{t}_{t1}$)= 32 $\mathbf{t}_{b2}$+ 28 ($\mathbf{t}_{b2}$-$\mathbf{t}_{b1}$). The results for a twist angle of $\theta \approx 1.1^\circ$ and a heterostrain value of $\epsilon = 0.1\%$ are shown in Supplementary Figure 4.

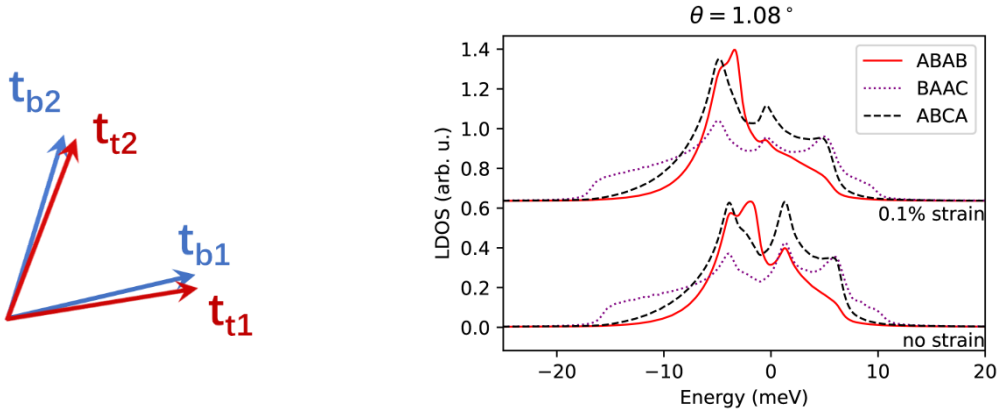

Supplementary Figure 4. Effect of heterostrain ($\epsilon = 0.1\%$) on the LDOS within the tight-binding model. Left: the lattice vectors of the top and the bottom two layers in the structure with heterostrain. The lattice vectors of the top two layers are indicated by the red arrows and the bottom two layers by the blue arrows. The lattice constant of the top two layers along $\mathbf{t}_{t2}$ is slightly expanded by 0.1% to create the structure with small heterostrain. Right: the experimentally observed shift to lower energies of the valence band in the BAAC regions is not reproduced by adding strain to the tight-binding model.

4. Functional Renormalization Group

The fRG treats interactions perturbatively in an unbiased way beyond mean-field by interpolating from the free system at high energies to an effective low-energy model. We use the truncated unity, intraorbital bilinear and Γ-point approximations from Ref. 9. Additionally, we include static self-energy effects consistent with the Γ-point and intraorbital bilinear approximations, motivated by the competition between symmetry breaking and non-symmetry breaking instabilities. Within these approximations, the vertex function $V^{\Lambda}_{o_1o_2o_3o_4}$ is split up into three channels (pairing, crossed particle-hole, direct particle-hole) that are matrices in unit cell index space:

$$P^{\Lambda}_{o_1o_2o_3o_4} = \delta_{o_1o_2}\delta_{o_3o_4}P^{\Lambda}_{o_1o_3}$$
$$C^{\Lambda}_{o_1o_2o_3o_4} = \delta_{o_1o_4}\delta_{o_2o_3}C^{\Lambda}_{o_1o_3} \qquad \textit{Eq. 3}$$
$$D^{\Lambda}_{o_1o_2o_3o_4} = \delta_{o_1o_3}\delta_{o_2o_4}D^{\Lambda}_{o_1o_2}$$

with

$$V^{\Lambda}_{o_1o_2o_3o_4} = P^{\Lambda}_{o_1o_2o_3o_4} + C^{\Lambda}_{o_1o_2o_3o_4} + D^{\Lambda}_{o_1o_2o_3o_4} \qquad \textit{Eq. 4}$$

The differential equations in the energy cutoff parameter Λ, which describe the renormalization group flow of a spin-degenerate system, read

$$\frac{d}{d\Lambda}\hat{P}^{\Lambda} = \hat{V}^{P_P,\Lambda}\dot{\hat{L}}^{PP,\Lambda}\hat{V}^{P_P,\Lambda}$$
$$\frac{d}{d\Lambda}\hat{C}^{\Lambda} = \hat{V}^{P_C},\Lambda\dot{\hat{L}}^{PH,\Lambda}\hat{V}^{P_C,\Lambda} \qquad \textit{Eq. 5}$$

$$\frac{d}{d\Lambda}\hat{D}^{\Lambda} = -2\hat{V}^{P_D,\Lambda}\dot{\hat{L}}^{PH,\Lambda}\hat{V}^{P_D,\Lambda} + \hat{V}^{P_D,\Lambda}\dot{\hat{L}}^{PH,\Lambda}\hat{V}^{P_C,\Lambda} + \hat{V}^{P_C,\Lambda}\dot{\hat{L}}^{PH,\Lambda}\hat{V}^{P_D,\Lambda}$$

All quantities are connected by matrix products. The channel projections of the vertex function are given by

$$\hat{V}^{P_P,\Lambda} = \hat{P}^{\Lambda} + diag\left(\hat{C}^{\Lambda}\right) + diag\left(\hat{D}^{\Lambda}\right)$$
$$\hat{V}^{P_C,\Lambda} = diag\left(\hat{P}^{\Lambda}\right) + \hat{C}^{\Lambda} + diag\left(\hat{D}^{\Lambda}\right) \qquad \textit{Eq. 6}$$
$$\hat{V}^{P_D,\Lambda} = diag\left(\hat{P}^{\Lambda}\right) + diag\left(\hat{C}^{\Lambda}\right) + \hat{D}^{\Lambda}$$

The particle-particle $\left(\hat{L}^{\mathrm{PP},\Lambda}\right)$ and particle-hole ($\hat{L}^{\mathrm{PH},\Lambda}$) loops within these approximations read

$$\hat{L}^{PP,\Lambda} = \int \frac{dk_0}{2\pi}\frac{1}{N}\sum_{\vec{k}} \hat{G}^{\Lambda}(k) \circ \hat{G}^{\Lambda}(-k)$$
$$\hat{L}^{PH,\Lambda} = \int \frac{dk_0}{2\pi}\frac{1}{N}\sum_{\vec{k}} \hat{G}^{\Lambda}(k) \circ \hat{G}^{\Lambda}(k) \qquad \textit{Eq. 7}$$

with $\hat{A} \circ \hat{B}$ the element-wise matrix product. For our fRG simulations, we use a sharp frequency cutoff of the Green's function that allows us to trivially carry out the Matsubara frequency integrals in the above equations:

$$\hat{G}^{\Lambda}(k) = \left(ik_0 - \hat{H}_0(k) - \hat{\Sigma}^{\Lambda} + \mu\right)^{-1}\Theta(|k_0| - \Lambda) \qquad \textit{Eq. 8}$$

We approximate the self-energy $\hat{\Sigma}^{\Lambda}$ as constant in momentum and frequency space. The matrix in orbital space then has to fulfil the flow equation

$$\frac{\mathrm{d}\Sigma_{ij}^{\Lambda}}{\mathrm{d}\Lambda} = S_{ij}^{\Lambda}\left[2C_{ij}^{\Lambda} - D_{ij}^{\Lambda}\right] + S_{ji}^{\Lambda}P_{ij}^{\Lambda} + \sum_{l}\left[2D_{il}^{\Lambda} - C_{il}^{\Lambda}\right]S_{ll}^{\Lambda}\delta_{ij} \qquad \textit{Eq. 9}$$

with the single-scale propagator

$$\hat{S}^{\Lambda} = \frac{\mathrm{d}}{\mathrm{d}\Lambda}\Big|_{\hat{\Sigma}^{\Lambda}\text{ fixed}} \int \frac{\mathrm{d}k_0}{2\pi}\frac{1}{N}\sum_{k} \hat{G}^{\Lambda}(k) \qquad \textit{Eq. 10}$$

Note that the Λ-derivatives $\dot{\hat{L}}^{\mathrm{PP},\Lambda}$ and $\dot{\hat{L}}^{\mathrm{PH},\Lambda}$ need to be carried out for $\hat{\Sigma}^{\Lambda}$ fixed as well. To avoid particle loss or accumulation during the fRG flow, we readjust the chemical potential at each flow step to correspond to the initial filling.

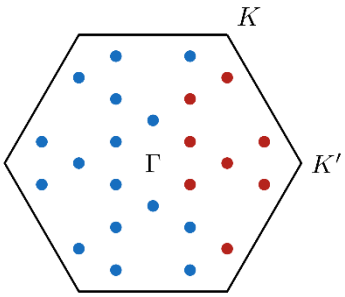

Supplementary Figure 4. Momentum mesh used in fRG simulations. Red points: meshing of irreducible Brillouin zone (IBZ); blue points and red points: meshing of full Brillouin zone. In order to reduce the computational effort required to obtain the particle-particle and particle-hole loops $\left(\hat{L}^{\mathrm{PP},\Lambda}\right.$ and $\left.\hat{L}^{\mathrm{PH},\Lambda}\right)$, we use the IBZ meshing and reconstruct the full loops using the in-plane C_3 symmetry.

The meshing of the momentum part of the integrals contains N = 24 points in the moiré Brillouin zone (see Supp. Fig. 4). We start the fRG flow at an energy cutoff of $\Lambda = 10$ eV and write the initial interaction in the direct particle-hole (D) channel. The chemical potential $\mu = \mu_n + 3.83$ meV corresponds to a partially filled conduction band, where μ_n is the chemical potential at charge neutrality. We set the filling to a half-filled conduction band (i.e., one electron more than charge neutrality per unit cell). During each step of the fRG flow, the leading eigenvalue of each interaction channel is determined and the stopping condition whether one of the eigenvalues is larger than $3 \cdot 10^2$ eV is evaluated. At the end of the flow, an eigendecomposition of the leading channel reveals the order parameters associated with the phase that the system will likely order in. Mean-field decoupling of the bilinears associated with the divergent channel enables us to determine single-particle properties in the ordered phase. The parameters presented here lead to a divergence in the D channel that points to a charge-modulation instability. We perform a mean-field decoupling of the (spin-independent) order parameter and arrive at the effective Hamiltonian (neglecting constants)

$$\mathcal{H}_{eff} = \mathcal{H}_0 + U_{eff} \sum_{k,i,\sigma} D_i^{\alpha} c_{k,i,\sigma}^{\dagger} c_{k,i,\sigma} \qquad \textit{Eq. 11}$$

The effective coupling strength U_{eff} remains unknown from our simulations, we set the *ad-hoc* value of $U_{\mathrm{eff}} = U$. The order parameter $\vec{D}^{\alpha}$ is the α -th eigenvector of the effective direct particle-hole channel and describes charge redistribution within the moiré unit cell.

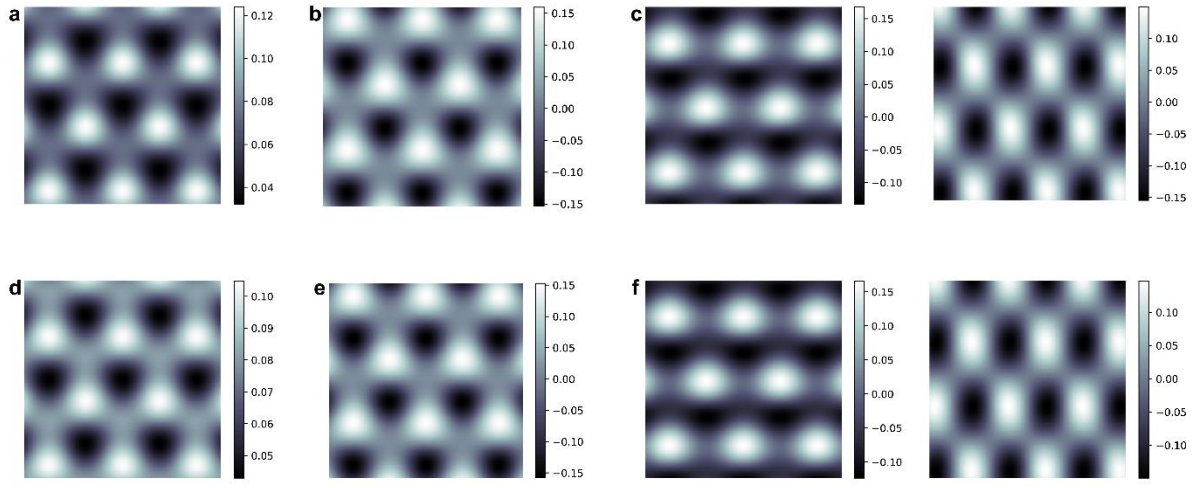

Supplementary Figure 5. Top layer projection of the three leading charge modulation orderings (leading eigenvectors) from our simulations for $U = 4$ eV and $r_c = 2a$. The first row (**a**, **b** and **c**) corresponds to RPA calculations and the second row (**d**, **e** and **f**) to the fRG result. The first two orderings, **a**/**d**, **b**/**e**, respect the lattice symmetries and manifest themselves as charge reordering within the moiré unit cell. The third ordering breaks the in-plane threefold rotational symmetry and consists of two degenerate eigenvectors shown in panels **c** and **f**. As the variation of the order parameter is on the moiré scale, it describes *moiré nematicity*.

The first two eigenvectors (orderings) respect the system's lattice symmetries whereas the third and fourth eigenvectors (degenerate eigenvalues) break C_3 (see Supp. Fig. 5). We note that in the fRG flow there are multiple closely competing orderings. The second and third orderings are weaker only by factors of 0.89 and 0.88 (for $U = 4$ eV). We find the same ordering tendencies for an RPA calculation with the same parameters with the only difference being a slight reduction in intensity of the third instability (from 0.88 to 0.87). The same orderings also appear when setting $U = 6$ eV or even $U = 8$ eV, neglecting self-energies and using a slightly different (sharp) interaction range cutoff function. Excluding self-energy effects slightly decreases the relative strength of the nematic instability, but in all of the checked configurations, it is well within 80% of the leading instability. All three leading ordering tendencies may strongly influence the physics at play and be visible experimentally. In the case of a degenerate eigenvalue (i.e. due to breaking a lattice symmetry), any linear combination of the two eigenvectors can be the order parameter. Due to the approximations made, it is possible that the closely competing orderings are interchanged making, e.g., moiré nematicity the leading instability. For the LDOS obtained from the effective Hamiltonian (shown in Fig. 4b in the main text), we use the first of the two degenerate eigenvectors (corresponding to the third eigenvalue) as the order parameter.

5. Nematic instability within the continuum model

The band structure of TDBG is well-described by the continuum model proposed in Ref. 14. We set the twist angle to be 1.05° and use the same model parameters as Ref. 14 with two exceptions. The first difference is that we take a rescaled band velocity of $\hbar v/a = 2.776$ eV. Secondly, instead of assuming a constant value for the interlayer asymmetric potential induced by the gate electric field, we use on-site potentials $\Delta_1 = 4.079$ meV, $\Delta_2 = 1.021$ meV, $\Delta_3 = -1.537$meV, and $\Delta_4 = -3.563$ meV for layers 1 through 4, respectively. This is done to self-consistently include the effect of the displacement field.
The nematic order can be described by a two-component order parameter $\mathbf{\Phi} = \Phi_0(\cos 2\theta, \sin 2\theta)$, with the angle θ characterizing the orientation of the nematic director[11]. The electronic degrees of freedom are described by the field operator $a_{\sigma,\ell,s,\tau}(\boldsymbol{r})$, with spin $\sigma = \uparrow, \downarrow$, sublattice s = 1,2, layer ℓ = 1, 2, 3, 4, valley $\tau = \pm$, and (continuum) position $\boldsymbol{r} \in \mathbb{R}^2$. While there are many ways of writing down the coupling between $\mathbf{\Phi}$ and the electronic degrees of freedom in the continuum model, we here focus on two opposing limiting cases, which we dub moiré nematic and graphene nematic[12]. The moiré nematic order parameter should be thought of as an anisotropic deformation of the effective nearest-neighbor hopping amplitudes on the moiré scale. Its coupling to the electrons is written as:

$$\mathcal{H}_{\boldsymbol{\Phi}} = \int d\boldsymbol{r} \sum_{R} \boldsymbol{\Phi} \cdot \boldsymbol{\phi}(\boldsymbol{r}, \boldsymbol{R})\, a^{\dagger}_{\sigma,\ell,s,\tau}(\boldsymbol{r}+\boldsymbol{R}) a_{\sigma,\ell,s,\tau}(\boldsymbol{r}) + H.c. \qquad \textit{Eq. 12}$$

where $\boldsymbol{R}$ denotes moiré lattice vectors. Restricting $\boldsymbol{R}$ to nearest neighbors and neglecting the $\boldsymbol{r}$ dependence of $\boldsymbol{\phi}$, this corresponds to a momentum-dependent shift of the spectrum $E_{n\boldsymbol{k}}$:

$$E_{n\boldsymbol{k}} \to E_{n\boldsymbol{k}} + \boldsymbol{\Phi} \cdot \boldsymbol{f}(\boldsymbol{k}), \quad \boldsymbol{f}(\boldsymbol{k}) \qquad \textit{Eq. 13}$$
$$= \frac{8}{3}\left(cos\, k_y - cos\frac{\sqrt{3}k_x}{2} cos\frac{k_y}{2}, \sqrt{3}\, sin\frac{\sqrt{3}k_x}{2} sin\frac{k_y}{2} \right)^T$$

Here, $\boldsymbol{k}$ denotes the momentum in the first moiré Brillouin zone, and n labels the bands of the continuum model without nematic order. As shown in Fig. 4 of the main text, upon setting $\Phi_0 = 1\text{meV}, \theta = \pi$, this model not only reproduces the experimentally observed stripes in the LDOS images, but also captures the splitting between the VFB peaks of the dI/dV curves at the ABAB, BAAC, and ABCA site positions.

In the case of the graphene nematic order parameter, nematicity occurs on the scale of the underlying graphene lattice. The simplest form of its coupling to the electrons is given by:

$$\mathcal{H}_{\Phi} = \int d\boldsymbol{r}\, \boldsymbol{\Phi} \cdot \begin{pmatrix} (\rho_x)_{ss'} \\ \tau(\rho_y)_{ss'} \end{pmatrix} a^{\dagger}_{\sigma,\ell,s,\tau}(\boldsymbol{r}) a_{\sigma,\ell,s',\tau}(\boldsymbol{r}) \qquad \textit{Eq. 14}$$

where we have made the reasonable assumption that the order parameter is trivial in spin space and does not possess any additional layer-hopping or layer-dependent component. Note that ρ_j, in the above expression, stands for Pauli matrices in the sublattice space. In Fig. 4 of the main text, we set $\Phi_0 = 20$ meV for the graphene nematic order parameter; note that even with this somewhat large value, the changes in the LDOS with respect to the non-nematic phase are nearly imperceptible.

6. The effect of strain on the LDOS

We can examine the effect of heterostrain on the spectrum of twisted double bilayer graphene within the context of the continuum model by generalizing the model studied in Ref. 13 to the case of four layers and applying a different uniaxial strain to each bilayer in the double-bilayer stack. We have included 0.1% heterostrain in our calculations with nonzero moiré nematic order, shown below for several values of strain angle. The strain tensor can be parametrized as[13]

$$\mathcal{S}_{ua} = R(\varphi)^{-1} \begin{pmatrix} -\epsilon & 0 \\ 0 & v\epsilon \end{pmatrix} R(\varphi)$$
$$= \epsilon \begin{pmatrix} -\cos(\varphi)^2 + v\sin(\varphi)^2 & (1+v)\cos(\varphi)\sin(\varphi) \\ (1+v)\cos(\varphi)\sin(\varphi) & -\sin(\varphi)^2 + v\cos(\varphi)^2 \end{pmatrix},$$

where ν = 0.16 is the Poisson ratio for graphene. Given our earlier choice of orientation of the nematic director θ = 0, the parameter φ represents the angle between the direction of the strain and the nematic director. When the strain is parallel or perpendicular to the nematic director, we still observe the site-dependent splitting of the valence flat band; however, we emphasize that this is due to the coexisting moiré nematic order and not due

to the strain itself. The inclusion of strain in the calculation does not improve the fit to experiment. In fact, for certain values of the strain angle (e.g., φ =π/4), we find that heterostrain can be inimical to the observation of nematic order, further supporting our claim that heterostrain is not driving the observed nematic phase.

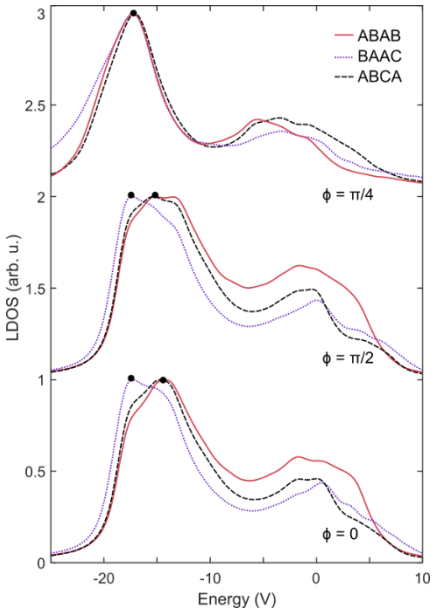

Supplementary Figure 6. 1.05° TDBG under the effect of heterostrain. Full continuum model DOS projected onto the top layer under 0.1 % heterostrain.

7. STS LDOS maps at charge neutrality and around half-filling

Below we show the STS LDOS maps at charge neutrality and around the half-filling doping condition showed in Fig. 2.

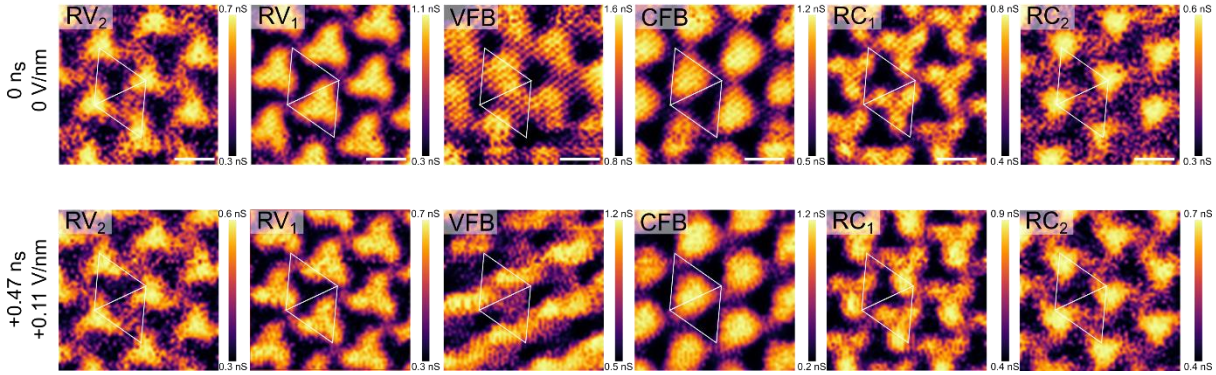

Supplementary Figure 7. STS LDOS maps for each of the bands, as indicated in the main text. Top (bottom) row correspond to charge neutrality (around half-filling).

8. Full energy range for large STS LDOS maps

Below we show the whole energy range for the STS LDOS maps around the half filling condition to complement the valence flat band map in Fig. 3b.

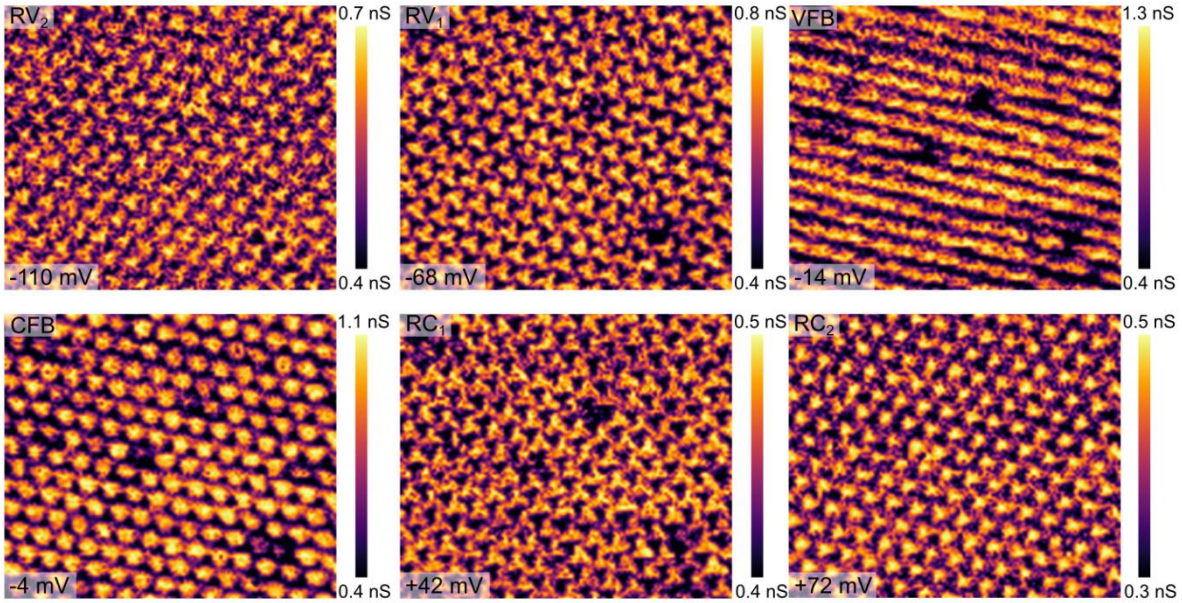

Supplementary Figure 8. Each panel corresponds to a STS LDOS map at each of the bands, as indicated in the main text. The energy is indicated in the bottom-left corner.

References

1. Fernandes, R. M., Chubukov, A. V & Schmalian, J. What drives nematic order in iron-based superconductors? *Nat. Phys.* **10**, 97–104 (2014).
2. Liu, S., Khalaf, E., Lee, J. Y. & Vishwanath, A. Nematic topological semimetal and insulator in magic-angle bilayer graphene at charge neutrality. *Phys. Rev. Res.* **3**, 013033 (2021).
3. Kumar, H., Dong, L. & Shenow, V. B. Limits of Coherency and Strain Transfer in Flexible 2D van der Waals Heterostructures: Formation of Strain Solitons and Interlayer Debonding. *Sci. Rep.* **6**, 21516 (2016).
4. Kerelsky, A. *et al.* Maximized electron interactions at the magic angle in twisted bilayer graphene. *Nature* **572**, 95–100 (2019).
5. Haddadi, F., Wu, Q., Kruchkov, A. J. & Yazyev, O. V. Moiré Flat Bands in Twisted Double Bilayer Graphene. *Nano Lett.* **20**, 2410'2415 (2020).
6. Plimpton, S. Fast parallel algorithms for short-range molecular dynamics. *J. Comput. Phys.* **117**, 1 (1995).
7. Brenner, D. W. *et al.* A secondgeneration reactive empirical bond order (rebo) potential energy expression for hydrocarbons. *J. Phys. Condens. Matter* **14**, 783 (2002).
8. Kolmogorov, A. N. & Crespi, V. H. Registry-dependent interlayer potential for graphitic systems. *Phys. Rev. B* **71**, 235415 (2005).
9. Bitzek, E., Koskinen, P., G ahler, F., Moseler, M. & Gumbsch, P. Structural relaxation made simple. *Phys. Rev. Lett.* **97**, 170201 (2006).
10. Wehling, T. O., S a s o glu, E., C. Friedrich, A. I. L., Katsnelson, M. I. & Blügel, S. Strength of effective coulomb interactions in graphene and graphite. *Phys. Rev. Lett.* **106**, 236805 (2011).
11. Fernandes, R. M. & Venderbos, J. W. F. Nematicity with a twist : Rotational symmetry

breaking in a moiré superlattice. *Sci. Adv.* **6**, 1–9 (2020).
12. Samajdar, R. *et al.* Electric-field-tunable electronic nematic order in twisted double-bilayer graphene. *2D Mater.* (2021).
13. Bi, Z., Yuan, N. F. Q. & Fu, L. Designing flat bands by strain. *Phys. Rev. B* **100**, 035448 (2019).